JACS
JOURNAL OF THE AMERICAN CHEMICAL SOCIETY
Article
pubs.acs.org/JACS

Toward Controlling Water Oxidation Catalysis: Tunable Activity of Ruthenium Complexes with Axial Imidazole/DMSO Ligands

Lei Wang,[†] Lele Duan,[†] Beverly Stewart,[‡] Maoping Pu,[‡] Jianhui Liu,*[,§] Timofei Privalov,*[,‡] and Licheng Sun*[,†,∥]

[†]Department of Chemistry, Royal Institute of Technology, 10044 Stockholm, Sweden

[‡]Department of Organic Chemistry, Arrhenius Laboratory, Stockholm University, 10691 Stockholm, Sweden

[§]State Key Laboratory of Fine Chemicals, Dalian University of Technology, Dalian 116024, P. R. China

[∥]State Key Laboratory of Fine Chemicals, DUT-KTH Joint Education and Research Center on Molecular Devices, Dalian University of Technology, Dalian 116024, P. R. China

Supporting Information

ABSTRACT: Using the combinations of imidazole and dimethyl sulfoxide (DMSO) as axial ligands and 2,2′-bipyridine-6,6′-dicarboxylate (bda) as the equatorial ligand, we have synthesized six novel ruthenium complexes with noticeably different activity as water oxidation catalysts (WOCs). In four C_s symmetric $Ru^{II}(\kappa^3\text{-bda})(DMSO)L_2$ complexes L = imidazole (**1**), *N*-methylimidazole (**2**), 5-methylimidazole (**3**), and 5-bromo-*N*-methylimidazole (**4**). Additionally, in two C_{2v} symmetric $Ru^{II}(\kappa^4\text{-bda})L_2$ complexes L = 5-nitroimidazole (**5**) and 5-bromo-*N*-methylimidazole (**6**), that is, fully equivalent axial imidazoles. A detailed characterization of all complexes and the mechanistic investigation of the catalytic water oxidation have been carried out with a number of experimental techniques, that is, kinetics, electrochemistry and high resolution mass spectrometry (HR-MS), and density functional theory (DFT) calculations. We have observed the in situ formation of a Ru^{II}-complex with the accessible seventh coordination position. The measured catalytic activities and kinetics of complex **1**−**6** revealed details about an important structure−activity relation: the connection between the nature of axial ligands in the combination and either the increase or decrease of the catalytic activity. In particular, an axial DMSO group substantially increases the turnover frequency of WOCs reported in the article, with the ruthenium-complex having one axial 5-bromo-N-methyl-imidazole and one axial DMSO (**4**), we have obtained a high initial turnover frequency of ~180 s^{-1}. DFT modeling of the binuclear reaction pathway of the O−O bond formation in catalytic water oxidation further corroborated the concept of the mechanistic significance of the axial ligands and rationalized the experimentally observed difference in the activity of complexes with imidazole/DMSO and imidazole/imidazole combinations of axial ligands.

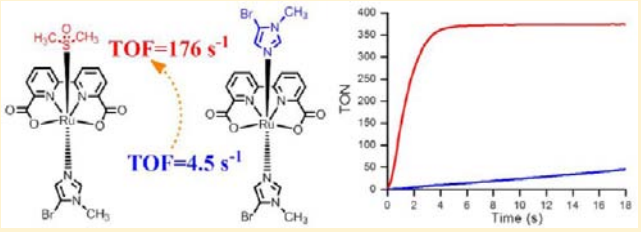

INTRODUCTION

Solar energy can be utilized for sustainable production of solar fuels using artificial photosynthesis for water splitting to hydrogen and oxygen.[1,2] As one-half of the total reaction, the importance of water oxidation to oxygen is that it provides necessary electrons and protons for the subsequent half reaction of hydrogen production.[3−8] Thereby a water oxidation catalyst (WOC) with high oxygen production rate is the critical component of the artificial photosynthetic system. "Blue Dimer" had been the first well characterized molecular catalyst for water oxidation.[9,10] Pursuit of a higher catalytic efficiency lead to the development of a number of WOCs and considerable progress in understanding of the reaction mechanism. Molecular catalysts for water oxidation with a much improved efficiency have been reported recently, such as complexes based on Co,[11−16] Ru,[17−31] Ir,[32−34] and Fe.[35] Mechanistic aspects of these WOCs have been investigated by electrochemical, kinetic and theoretical studies.[36−45] Recently, promising results using photoelectrochemical cells (PECs) with WOCs attached at the photoanodes have been reported.[46−50] However, to bring the performance of PEC to the practically viable level, a substantial increase of the rate of hole scavenging, in comparison with the rate of electron's back transfer, is necessary. In practical terms, a WOC with much a higher oxygen producing rate is necessary. This brings us to the point of our study since designing of both high performing and chemically stable WOC requires thorough knowledge of structure−activity relationships.

Recently, some WOCs based on earth abundant metals have been reported with moderate catalytic activity,[35] nonetheless a better comprehension of fundamental principles of ligand-design is required in order to apply present success with ruthenium complexes on earth abundant metals. Earlier, we

Received: October 10, 2012
Published: October 12, 2012

 © 2012 American Chemical Society dx.doi.org/10.1021/ja309805m | J. Am. Chem. Soc. 2012, 134, 18868−18880

Scheme 1. Molecular Structures of 1−7[a]

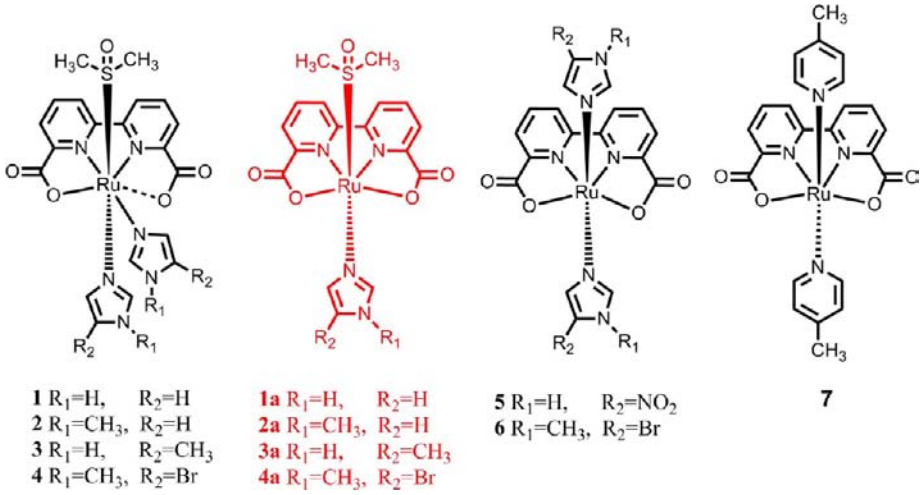

[a]Complexes **1**−**4** readily lose the equatorial imidazoles in solutions to form complexes **1a**−**4a**, more details in the discussion part.

have demonstrated that relatively minor modification of the equatorial ligand backbone leads to a significant change in the kinetics of water oxidation.[23] Recently, we discovered that an alternation of axial ligands, that is, two isoquinolines as axial ligands instead of two picolines, leads to an unprecedentedly high increase of the reaction rate, that is, turn over frequency (TOF), of the catalytic water splitting with Ru(bda)L_2 complex.[51] This prompted us to look deeper at the effect axial ligands could have on the catalytic activity of Ru(bda)L_2 complexes. Ruthenium-based WOCs bearing a negatively charged ligand 2,2'-bipyridine-6,6'-dicarboxylate (bda) which can stabilize the high-valent ruthenium have been reported by our group.[17,41] The highest turnover frequency (TOF) of this family of catalysts is about 300 s^{-1},[51] currently a record to the best of our knowledge.[35,52] Considering the success of Ru-bda WOCs, we went on to synthesize a series of Ru-bda complexes using new axial ligands. Considering that imidazole is (i) a part of many important biological molecules (ii) similar to pyridine-based ligands in terms of metal-coordination properties, (iii) directly adjustable using a variation of substituents, and (iv) more electron-donating ligand compared with pyridine (a desirable trait to lower the oxidation potential of the resulting Ru-bda complexes even further), we thereby synthesized a series of Ru-bda complexes, bearing imidazole ligands with imidazole (**1**), *N*-methylimidazole (**2**), 5-methylimidazole (**3**), and 5-bromo-*N*-methylimidazole (**4**). For complexes **1**−**4**, one DMSO (DMSO = dimethyl sulfoxide) appeared coordinated to the ruthenium ion becoming one of the two axial ligands. Additionally, we synthesized ruthenium complexes with L = 5-nitroimidazole (**5**), and *N*-methyl-5-bromoimidazole (**6**), which do not contain DMSO as the control complexes. Details are provided in Scheme 1. Herein, we report the synthesis of complexes **1**−**6**, spectroscopic characterization, electrochemical properties, and mechanistic investigation of the water oxidation catalysis in combination with theoretical calculations.

Thus far according to the literature, a vast majority of (axial) ligands have nitrogen as donor atoms. An important, in our opinion, element of novelty of our work is that hetero (or nonequivalent) axial ligands (imidazole/DMSO) versus homo (or totally equivalent) axial ligands (imidazole/imidazole) have not been compare although the idea is appealing from the purely synthetic and the mechanistic viewpoints. It is of novelty to have a WOC with a ligand that has actually not one but two non-nitrogen donor atoms, sulfur and oxygen which are more suitable to support different oxidation states of the ruthenium center alongside the concept of hard/soft donor−acceptor ligand interactions

EXPERIMENTAL SECTION

Materials and Synthesis. All chemicals and solvent, if not stated otherwise, were purchased from Sigma-Aldrich without further purification, *N*-bromosuccinimide (NBS) was purified before use, 2,2'-bipyridine-6,6'-dicarboxylic acid (H_2bda) was purchased from Jinan Henghua Sci. & Tec. Co. Ltd., *cis*-[Ru(DMSO)$_4$Cl$_2$], complex **7** and 5-bromo-*N*-methyl-imidazole were synthesized following literature methods.[17,53,54] The ^{1}H NMR spectra were recorded on a 400 MHz NMR of Bruker Avance spectrometer with TMS as internal standard. Mass spectra were performed by electrospray ionization (ESI) on an HP 1100 MSD instrument. Elemental analyses were performed with a Thermmoquest-Flash EA 1112 apparatus.

*Synthesis of [Ru^{II}(κ^3-bda)(imidazole)$_2$(DMSO)] (**1**).* A mixture of 2,2′-bipyridine-6,6′-dicarboxylic acid (H_2bda) (244 mg, 1.0 mmol), *cis*-[Ru(DMSO)$_4$Cl$_2$] (484 mg, 1.0 mmol), and Et_3N (0.8 mL) in methanol (20 mL) was degassed with N_2 and refluxed over 3 h. An excess of imidazole was added and the reflux was continued for additional 16 h. Solvents were then removed, and the resulting mixture was purified by column chromatography on silica gel using methanol as eluents, yielding **1** as a dark red solid (yield = 36%). ^{1}H NMR (400 MHz, D_2O): δ = 8.27 (d, J = 8.0 Hz, 1H), 8.14 (d, J = 8.0 Hz, 1H), 8.04 (s, 1H), 7.91 (m, J = 8.0 Hz, 3H), 7.37 (d, J = 8.0 Hz, 1H), 7.13 (s, 1H), 7.01(s, 1H), 6.92(s, 1H), 6.76(s, 1H), 6.21(s, 1H), 2.60(d, J = 8.0 Hz, 6H). TOF HR MS-ES$^+$: m/z^+ = 559.0325 (M + H$^+$), calcd 559.0338. Elemental analysis: Calcd. for 96.5% **1** ($C_{20}H_{20}N_6O_5RuS$) with 3.5% **1a** ($C_{17}H_{16}N_4O_5RuS$) C, 42.96; H, 3.59; N, 14.76. Found: C, 42.89; H, 3.45; N, 15.01.

Similar procedures as described for **1** were followed using imidazole derivatives instead of imidazole to afford the corresponding complexes **2**, **3**, **4**, and **5**.

*[Ru^{II}(κ^3-bda)(N-methylimidazole)$_2$(DMSO)] (**2**).* Compound **2** was obtained as dark red solid (yield = 32%). ^{1}H NMR (400 MHz, D_2O): δ = 8.28 (d, J = 8.0 Hz, 1H), 8.16 (d, J = 8.0 Hz, 1H), 7.93 (m, J = 8.0 Hz, 4H), 7.05 (d, J = 8.0 Hz, 1H), 6.96 (s, 1H), 6.90(s, 1H), 6.75(s, 1H), 6.71(s, 1H), 6.20(s, 1H), 3.62(s, 3H),3.32(s, 3H), 2.65(d, J = 8.0 Hz, 6H). TOF HR MS-ES$^+$: m/z^+ = 587.0665 (M + H$^+$), calcd 587.0651. Elemental analysis: Calcd. for 94% **2**($C_{22}H_{24}N_6O_5RuS$) with 6% **2a** ($C_{18}H_{18}N_4O_5RuS$) C, 44. 77; H, 4.13; N, 14.12. Found: C, 44.97; H, 3.99; N, 14.26.

[Ru^{II}(κ^3-bda)(5-methylimidazole)$_2$(DMSO)] (**3**). Compound **3** was obtained as dark red solid (yield = 34%). ^{1}H NMR (400 MHz, D_2O): δ = 8.21 (t, J = 8.0 Hz, 1H), 8.10 (d, J = 8.0 Hz, 1H), 7.89 (m, J = 8.0 Hz, 4H), 7.34 (d, J = 8.0 Hz, 1H), 6.94 (s, 1H), 6.57(s, 1H), 5.85(s, 1H), 2.62(d, J = 8.0 Hz, 6H), 2.01(s, 3H), 1.76(s, 3H). TOF HR MS-ES$^+$: m/z^+ = 587.0673 (M + H$^+$), calcd 587.0651. Elemental analysis: Calcd. for 95% **3** ($C_{22}H_{24}N_6O_5RuS$) with 5% **3a** ($C_{18}H_{18}N_4O_5RuS$) C, 44.54; H, 4.02; N, 13.77. Found: C, 44.72; H, 4.12; N, 14.04.

[Ru^{II}(κ^3-bda)(5-bromo-N-methylimidazole)$_2$(DMSO)] (**4**). Compound **4** was obtained as dark red solid (yield = 39%). ^{1}H NMR (400 MHz, D_2O): δ = 8.25 (t, J = 8.0 Hz, 1H), 8.12 (d, J = 8.0 Hz, 1H), 8.09 (s, 1H), 7.92 (m, J = 8.0 Hz, 3H), 7.36 (d, J = 8.0 Hz, 1H), 7.19 (s, 1H), 6.89 (s, 1H), 6.24 (s, 1H), 3.51(s, 3H), 3.20(s, 3H), 2.58(s, 6H). TOF HR MS-ES$^+$: m/z^+ = 744.8862 (M + H$^+$), calcd 744.8840. Elemental analysis: Calcd. for 96% **4** ($C_{22}H_{22}Br_2N_6O_5RuS$) with 4% **4a** ($C_{18}H_{17}BrN_4O_5RuS$) C, 35.65; H, 2.97; N, 11.18. Found C, 35.19; H, 2.77; N, 11.14.

[Ru^{II}(κ^4-bda)(5-nitroimidazole)$_2$] (**5**). Compound **5** was obtained as dark red solid (yield = 31%). ^{1}H NMR (400 MHz, D_2O): δ = 8.18 (d, J = 8.0 Hz, 2H), 7.78 (d, J = 8.0 Hz, 2H), 7.69 (t, J = 8.0 Hz, 2H), 7.26 (s, 2H), 6.98 (s, 2H), 6.57(s, 2H). TOF HR MS-ES$^+$: m/z^+ = 570.9936 (M + H$^+$), calcd 570.9900. Elemental analysis: Calcd. for $C_{18}H_{12}N_8O_8Ru$ C, 37.97; H, 2.12; N, 19.68. Found: C, 37.62; H, 2.01; N, 19.38.

[Ru^{II} (κ^4-bda)(N-methyl-5-bromoimidazole)$_2$] (**6**). A mixture of 2,2′-bipyridine-6,6′-dicarboxylic acid (H_2bda) (122 mg, 0.5 mmol), $RuCl_3\cdot 3H_2O$ (130 mg, 0.5 mmol), and Et_3N (0.4 mL) in methanol (10 mL) and ethanol (20 mL) was degassed with N_2 and refluxed over 2 h. An excess of *N*-methyl-2-bromoimidazole (640 mg, 4 mmol) was added and the reflux was continued for additional 10 h. The solvent was removed, and the mixture purified by column chromatography on silica gel using methanol as eluents. Compound **2** was obtained as dark pink solid (yield = 12%). ^{1}H NMR (400 MHz, D_2O): δ = 8.41 (d, J = 8.0 Hz, 2H), 8.12 (d, J = 8.0 Hz, 2H), 7.83 (t, J = 8.0 Hz, 2H), 7.30 (s, 2H), 6.26 (s, 2H), 3.50 (s, 6H). TOF HR MS-ES: m/z^+= 688.8516 (M + Na$^+$), calcd 688.8521. Elemental analysis: Calcd. for $C_{20}H_{16}Br_2N_6O_4Ru$ C, 36.11; H, 2.42; N, 12.63. Found: C, 35.93; H, 2.18; N, 12.39.

Physical Methods. Cyclic voltammetry (CV) and differential pulse voltammetry (DPV) measurements were carried out with an Autolab potentiostat with a GPES electrochemical interface (Eco Chemie), using pyrolytic graphite electrode (basal plane, diameter 3 mm) (PGBE) as the working electrode, a platinum column as the counter-electrode, and an Ag/AgCl electrode (3 M KCl aqueous solution) as the reference electrode. The cyclic volatmmograms were obtained in a CF_3SO_3H aqueous solution (pH = 1.0). With $[Ru(bpy)_3]^{2+}$ ($E_{1/2}(Ru)^{III/II}$ = 1.26 V versus NHE) as an internal reference, potentials reported herein are referenced to a normal hydrogen electrode (NHE).

Kinetic experiments were carried out by Stopped-flow (Biologic SFM-300 and 400) double-mixing stopped flow system equipped with a diode array detector. Ce^{IV} in pH 1.0 solutions for kinetic and stoichiometric measurements were prepared from $(NH_4)_2Ce(NO_3)_6$ (99.99+%, Aldrich) and nitric acid (trace metal grade, 70%, purified by redistillation, 99.999%, Fisher Scientific).

The oxygen evolution data was monitored by a pressure transducer (Omega PX138-030A5 V) driven by a power supply (TTi-PL601) at 8.00 V versus time, then the amount of oxygen was calibrated by GC (GC-2014 Shimadzu). First, the solution of $(NH_4)_2[Ce(NO_3)_6]$(Ce^{IV}) in 0.1 M CF_3SO_3H (3.2 mL) was added into the flask, then the aqueous of the catalyst (20−400 μL, 2 mM) were injected into the above solution under vigorous stirring at ambient temperature (21 ± 1 °C). Second, 500 μL gas phase measurement by Gas chromatography (GC) (the oxygen in air was detracted). The end-point oxygen generated was converted to TON as report.

Suitable single crystals from the dichloromethane solution of complex **4** were obtained by diffusion technique. X-ray crystal determination of **4**(**4a**) was carried out with Bruker-Nonius KappaCCD with MoKα at 173 K in order to prevent decomposition of the solvate. The crystallographic data information is listed in Supporting Information Table S1.

RESULTS AND DISCUSSION

Synthesis and Structure. [Ru(κ^4-bda)(picoline)$_2$] complexes have been reported as WOCs with promising efficiency.[17] In order to reduce the overpotential of this family of catalysts, as well as for additional reasons mentioned in Introduction, we introduced imidazole and its derivatives to the ruthenium complexes as axial ligands. Following the synthetic procedure as described for [Ru(κ^4-bda)(picoline)$_2$],[17] we expected to obtain C_{2v} symmetric complexes with the molecular formula Ru(κ^4-bda)L_2. Using 5-nitroimidazole, we have indeed obtained complexes of the type Ru(κ^4-bda)L_2 with the pair of equivalent imidazoles in axial positions. For other imidazole derivatives intended as axial ligands, C_s asymmetric complexes of the type Ru(κ^3-bda)(DMSO)L_2, **1**−**4**, were obtained (see Scheme 1) a DMSO coordinate to ruthenium at one of axial positions. Complexes **1**−**4** were fully characterized by NMR spectroscopy, mass spectrometry and elementary analysis. All structures are summarized in Scheme 1 based on NMR data (Figure 1 and Supporting Information Figure S1) and MS

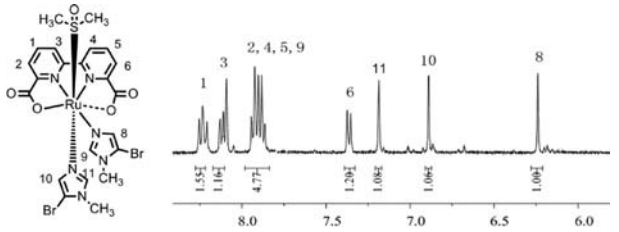

Figure 1. Low-field ^{1}H NMR spectrum of complex **4** in CD_3OD, highlighting its asymmetrical structure.

spectra. Figure 1 shows the ^{1}H NMR spectrum of complex **4**. The molecule has an apparent low symmetry with all of the signals of the aromatic protons dispersed with different chemical shifts: four peaks at 8.25 (t, 1H), 8.12 (d, 1H), 7.92 (m, 3H), and 7.36 (d, 1H) are contributed by the protons of bda^{2-}.

Complexes **1**−**4** readily lose the equatorial imidazoles in solutions (both methanol and water), transforming to complexes **1a**−**4a** with an accessible seventh coordination site on ruthenium. We noticed that the transformation process from **1**−**4** to **1a**−**4a** becomes very fast under acidic conditions in aqueous solutions which are typical for water oxidation catalysis driven by Ce^{IV}. Figure 2a displays the ^{1}H NMR spectrum of **4a** generated in situ after an addition of **4** in the pH 1.0 aqueous solution. Complex **4** transforms entirely into C_{2v} **4a** in acidic conditions. The dissociated imidazole ligand was also identified in the ^{1}H NMR spectrum (peaks 6 and 7 in Figure 2a) in an agreement with the spectrum of the pure imidazole ligand (Figure 2b). Similarly, complexes **1**−**3** transform completely into **1a**−**3a** in acidic aqueous (see Supporting Information Figure S2).

Complete loss of (equatorial) imidazole in acidic solution also has been confirmed using mass spectrometric analysis in neutral aqueous and pH 1.0 solutions (0.1 M CF_3SO_3H) respectively, as show in Figure 3. In neutral conditions, the peak at m/z = 744.58 was assigned to the [M + H]$^+$ species of **4** (calcd 744.8840). In the acid solutions this peak was not observed. Instead, only the species of [M−imd + H]$^+$ (imd =5-

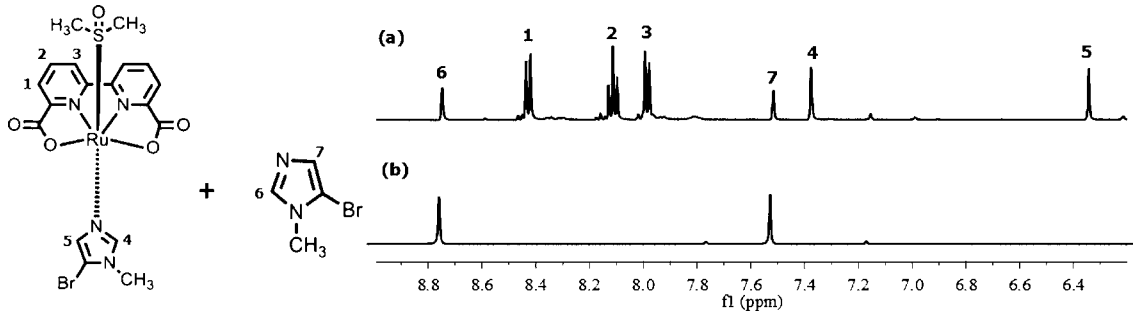

Figure 2. Low-field ^{1}H NMR spectra of (a) complex **4a** generated in situ from **4** and (b) 5-bromo-*N*-methylimidazole both in pH 1.0 aqueous (0.1 M CF_3SO_3D in D_2O with a small amount of ascorbic acid as a reducing reagent). Note: Proton resonance peaks 1−3 belong to L, two protons in imidazole resonance at 4 and 5, and peaks 6 and 7 belong to the free imidazole ligand which was released from complex **4**.

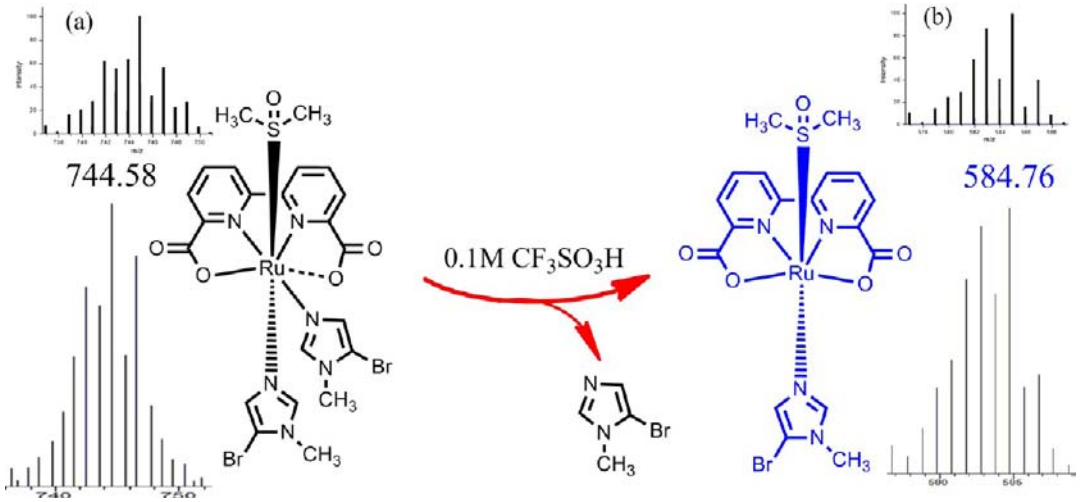

Figure 3. Mass spectra of **4** in neutral water and **4a** generated in situ from **4** in a pH 1.0 aqueous solution, with the simulated patterns for **4** (a) and **4a** (b).

bromo-N-methylimidazole; calcd 584.9204 and found 584.76) was detected, confirming the transformation of **4** into **4a** and a free imidazole.

Suitable single crystals were obtained from a solution of **4**. The resolved X-ray structure revealed Ru(κ^4-bda)(5-bromo-*N*-methylimidazole)(DMSO) complex (**4a**). The perspective view of **4a** is shown in Figure 4. As expected, the Ru^{II} is in an octahedral configuration with the N, N, O, O atoms of the square planar 2,2′-bipyridine-6,6′-dicarboxylate in the equatorial plane, and a DMSO ligand, as well as an imidazole ligand in the axial positions. The DMSO is bound to ruthenium through sulfur and trans to imidazole. The O2−Ru1−O3 bite angle of **4a** is slightly bigger than that of previously reported complex [Ru(κ^4-bda)(picoline)$_2$] (**7**), although the difference is small, just 1.7°. The X-ray structural data clearly shows that the seventh coordination site is available in **4a**, suggesting that in solution it should also be readily accessible for a coordination of a small solvent molecules such as water; larger O2−Ru1−O3 bite angle of complex **4a** in comparison with that of **7** should in principle make ruthenium even more accessible (see below).

When 5-nitroimidazole was employed as a coligand, complex **5** [Ru(κ^4-bda)(5-nitroimidazole)$_2$] was obtained instead of [Ru(κ^3-bda)(5-nitroimidazole)$_2$(DMSO)], confirmed by ^{1}H NMR spectrum (Supporting Information Figure S3), which is in agreement with the C_{2v} symmetric complex **5**. In addition, the MS measurements of **5** showed no DMSO-containing fragments. Also, the C_{2v} symmetric Ru (κ^4-bda)(5-bromo-*N*-methylimidazole)$_2$ complex (**6**), similar to **5**, was prepared by reacting $RuCl_3{\cdot}3H_2O$ and H_2bda, followed by addition of the excess 5-bromo-*N*-methylimidazole ligand.

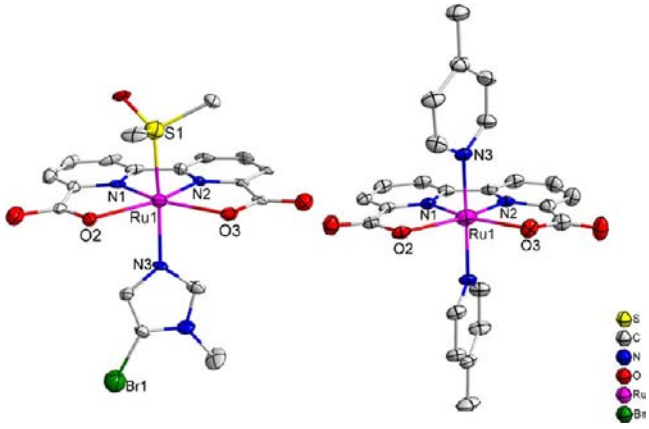

Figure 4. Left: X-ray crystal structure of complex **4a** with thermal ellipsoids at 50% probability (hydrogen atoms are omitted for clarity). Selected bond lengths (Å) and angles (deg): N1−Ru1 1.979, N2−Ru1 1.922, N3−Ru1 2.131, S1−Ru1 2.242, O2−Ru1 2.208, O3−Ru1 2.203, N1−Ru1−O2 77.20, N2−Ru1−N1 81.49, N2−Ru1−O3 76.54, O2−Ru1−O3 124.69. Right: The X-ray crystal structure of complex **7** reported previously with O2−Ru1−O3 = 122.99.[17]

Electrochemistry. Electrochemical properties of complexes **1**−**6** in aqueous solutions are important for a better

dx.doi.org/10.1021/ja309805m | J. Am. Chem. Soc. 2012, 134, 18868−18880

understanding of their catalytic properties and determining their onset potentials of the catalytic water oxidation. Table 1 summarizes the electrochemical data measured for complexes **1**–**6** in pH 1.0 solutions. Redox properties have been investigated using differential pulse voltammetry (DPV) and cyclic voltammetry (CV). Taking into account a complete loss of equatorial imidazoles in complexes **1**–**4** in pH 1.0 solution, the herein reported redox potentials should correspond to complexes **1a**–**4a**. For sake of space, we only show results for complexes **4** and **6** (Figure 5). In pH 1.0 (0.1 M CF_3SO_3H) solution, the redox potentials of $Ru^{III/II}$ and $Ru^{IV/III}$ couples of **4a** appear at 0.91 and 1.14 V, respectively, both versus NHE. A small wave at 1.40 V versus NHE was assigned to $Ru^{V/IV}$ couple (Figure 5a). CV of **4a** was measured under the same conditions (Figure 5b), showing two reversible waves of $Ru^{III/II}$ and $Ru^{IV/III}$ redox couples, and a large catalytic current starting from 1.5 V. In addition, a wave at −0.25 V is observed corresponding to the reduction of electrochemically generated O_2. The $Ru^{III/II}$ and $Ru^{IV/III}$ couples of **6** appear at 0.70 and 1.08 V, respectively. These values are lower than those of **4a** because the S-coordinated DMSO ligand is less electron donating ligand compared with the imidazole ligand.

Figure 6 displays the Pourbaix diagram of complex **4a** generated in situ from complex **4** due to the loss of the equatorial imidazole. A pH-independent one electron oxidation wave corresponding to the $Ru^{III/II}$ process of the Ru aqua complex appears at 0.92 V over a pH range of 0–5.7, indicating that the pK_a value of Ru^{III}–OH_2 is 5.7. A well-defined line with slope close to 59 mV/pH was found from pH 5.7 to 8 (no data was collected at higher pH values than pH 8 due to the decomposition of **4a**), corresponding to a $1e^-/1H^+$ proton coupled electron transfer (PCET) process of Ru^{II}–OH_2 to Ru^{III}–OH. The $Ru^{III/IV}$ process is a typical one electron one proton PCET process over the whole pH range from 1 to 8. Further oxidation of Ru^{IV}–OH to formally Ru^{V}=O is accompanied by one proton transfer as expected, while the

Table 1. Cyclic Voltammogram, TON and TOF data of 1–7[a]

complex	$E_{1/2}^{ox}$. (V vs NHE[b]) Ru(II/III)	Ru(III/IV)	Ru(IV/V)	E_{onset} (V)[c]	TON[d]	TOF[e] (s^{-1})
1(**1a**)	0.90	1.15	1.39	1.45	2032	137.6
2(**2a**)	0.89	1.13	1.37	1.43	2365	146.2
3(**3a**)	0.92	1.14	1.38	1.44	550	150.8
4(**4a**)	0.91	1.14	1.40	1.46	4050	176.5
5	0.68	1.05		1.34	1094	3.4
6	0.70	1.08		1.35	1150	4.5
7	0.86	1.11		1.50	2000	41.2

[a]Measured in pH 1.0 solution (0.1 M CF_3SO_3H). Scan rate = 0.1 V/s. [b]$[Ru(bpy)_3]^{2+}$ was used as a reference with $E_{1/2}$ = 1.26 V vs NHE. [c]The onset potential of catalytic curve. [d]Conditions: catalyst (1.20×10^{-5} M, 3.60×10^{-8} mol for **1**–**4**; 2.99×10^{-5} M, 1.01×10^{-7} mol for **5** and **6**) and Ce^{IV} (0.4 M) in 3.3 mL CF_3SO_3H aqueous solutions. [e]Conditions: catalyst (2.16×10^{-4} M, 7.99×10^{-7} mol **1**–**7**) and Ce^{IV} (0.4 M) in 3.7 mL CF_3SO_3H aqueous solutions.

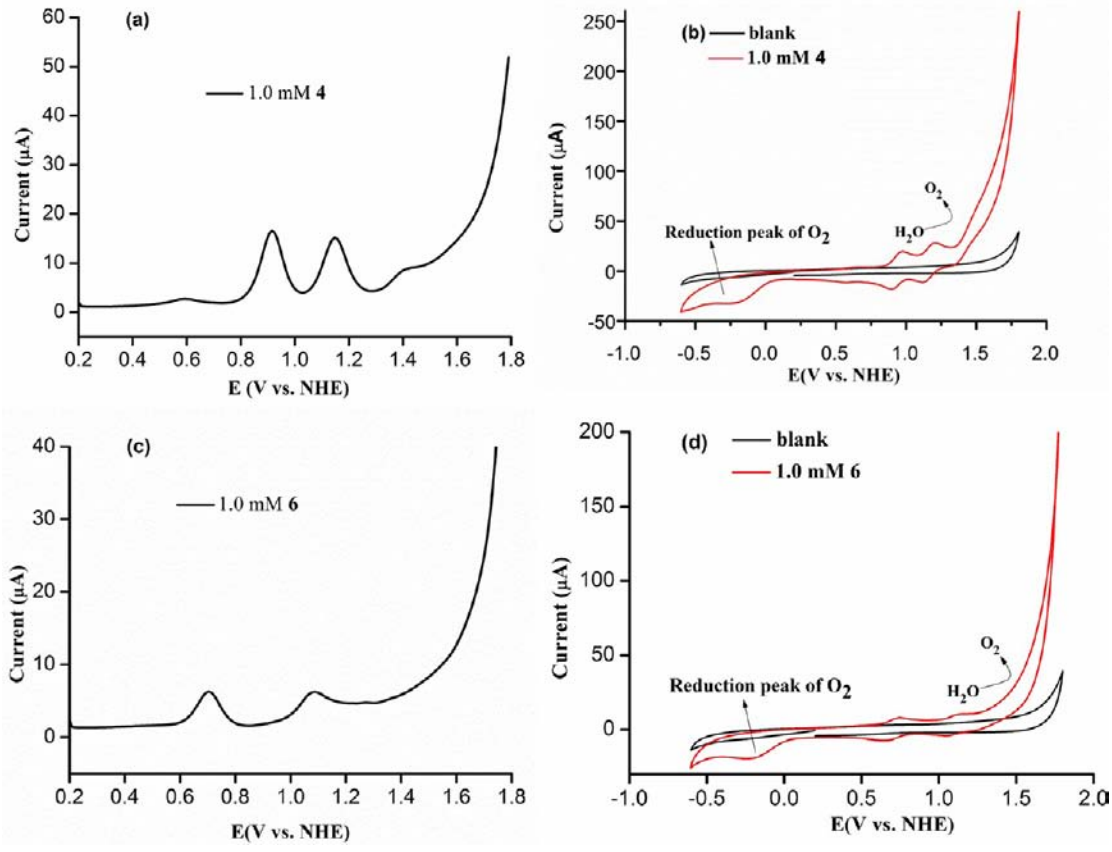

Figure 5. (a) DPV of **4a** generated in situ by dissolving **4** in a pH 1.0 solution. (b) Comparison of CVs in the absence (black curve) and presence (red curve) of **4a**. (c) DPV of **6**. (d) Comparison of CVs in the absence (black curve) and presence (red curve) of **6**. Conditions for all of the electrochemistry experiments: scan rate, 0.1 V/s; working electrode, PGBE; counter electrode, Pt column; reference electrode, Ag/AgCl.

dx.doi.org/10.1021/ja309805m | J. Am. Chem. Soc. 2012, 134, 18868–18880

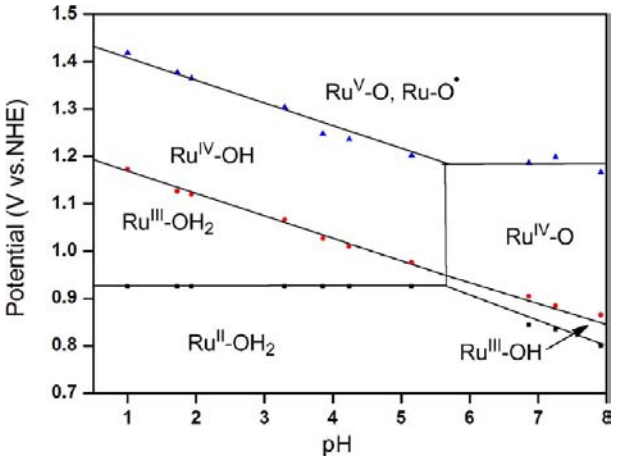

Figure 6. Plots of *E* versus pH (Pourbaix diagram) for complex **4a** in phosphate buffer.

oxidation of Ru^{IV}═O obviously involves only electron transfer. Accordingly, the reaction processes of **4a** under pH 1.0 conditions could be summarized as following: $Ru^{II}-OH_2 \rightarrow Ru^{III}-OH_2 \rightarrow Ru^{IV}-OH \rightarrow Ru^{V}$═O.

Catalytic Activity. Chemical water oxidation has been demonstrated by using Ce^{IV} as oxidant in pH 1.0 aqueous. The curve of oxygen evolution has been obtained using a pressure transducer using GC to calibrate the amount of generated O_2. All the catalytic data were collected in Table 1. From the point of the effectiveness as catalysts (both TON and TOF, see Table 1), complexes **1**−**4** (**1a**−**4a**) with the axial DMSO are better than complexes **5** and **6** which do not contain a DMSO axial ligand. Complex **4** gives a TOF of 176.5 s^{-1} for oxygen generation at [**4**] = 2.16×10^{-4} M, while **5** and **6** display TOFs of 3.4 and 4.5 s^{-1}, respectively, under the same conditions. After decreasing the concentration of catalyst to 1.20×10^{-5} M, a high TON of 4050 was observed for **4** (**4a**), and a moderate TON of 550 for **3** (**3a**). Under the same test conditions, complex **7** was measured as the reference and a TON of 2000 was obtained. Complex **4** reached a high TOF value of 176.5 s^{-1} at [**4**] = 2.16×10^{-4} M, which is much larger than the TOF of **6** (4.5 s^{-1}). The only difference between **4** and **6** is the presence of DMSO instead one of the imidazole ligands. More discussions about the influence at efficiency by DMSO group are in the DFT Calculations part.

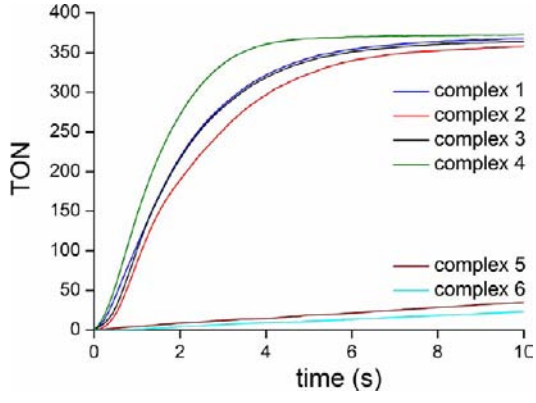

Figure 7. Kinetic curves of O_2 formation by complexes **1**−**6** vs time under conditions: 3.3 mL of pH = 1.0 aqueous (0.1 M CF_3SO_3H) containing 0.4 M Ce^{IV} and 2.16×10^{-4} M catalyst.

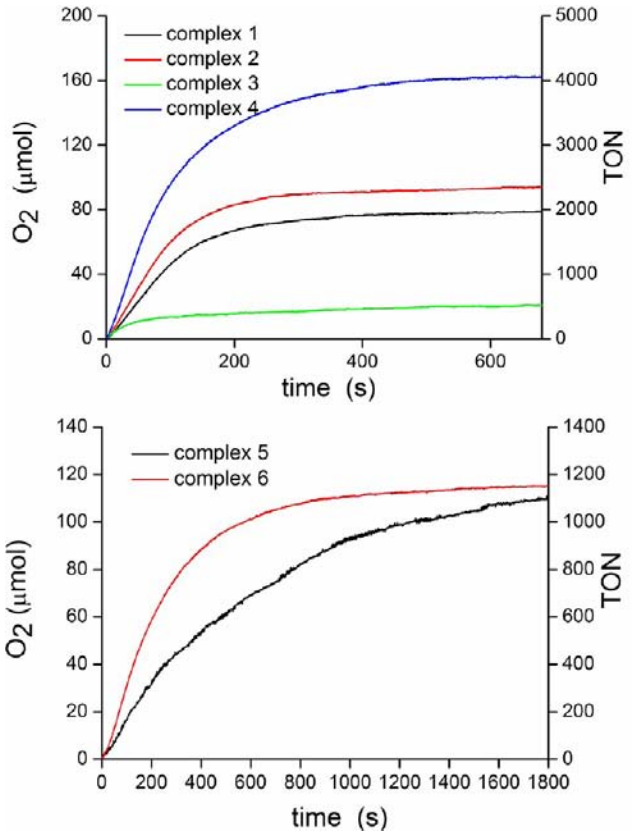

Figure 8. Kinetic curves of O_2 formation by complexes **1**−**6** vs time under conditions: pH = 1.0 aqueous (0.1 M CF_3SO_3H) 3.3 mL containing 0.4 M Ce^{IV} and 1.20×10^{-5} M complexes **1**−**4**, 2.99×10^{-5} M complexes **5** and **6**, respectively.

Seven-Coordinate Intermediate. To analyze the intermediates involved in the catalytic water oxidation, HR-MS measurements of the reaction mixture were performed with capillary temperature of 175 °C. Similar to our previous observations, a seven coordinate $Ru^{IV}-OH$ species has been detected.[17] For example, using complex **6** as a catalyst, the $[Ru^{IV}-OH]^+$ was found at m/z^+ = 682.8622, which fits well with the calculated value of m/z^+ = 682.8650 (as show in Figure 9).

Kinetic Study. To understand the kinetics of Ce^{IV}-driven water oxidation by Ru-bda complexes, we carried out the kinetic measurements monitoring the decay of Ce^{IV} at 360 nm in aqueous solutions (pH = 1.0, 0.1 M HNO_3). Figure 10 shows the kinetic data using complex **4** as a catalyst. The rate law of Ce^{IV} consumption is first order in Ce^{IV} under low [Ce^{IV}] conditions ([Ce^{IV}] < 2.0 mM; k = 0.124 s^{-1}) and zeroth-order in Ce^{IV} under high [Ce^{IV}] conditions ([Ce^{IV}] > 2.0 mM), while it is second order in catalyst **4** ($k = 1.86 \times 10^8$ $M^{-1}s^{-1}$). Similar to $[Ru(bda)L_2]$ (L = picoline and isoquinoline),[51] water oxidation catalyzed by **4a**, we propose according to the second order nature, also involves the radical coupling of two Ru^{V}═O (Ru^{V}═O ↔ $Ru^{IV}-O^{\bullet}$) species being the O−O bond formation step, that is, 2 × Ru^{V}═O → $Ru^{IV}-O-O-Ru^{IV}$.[51] A much smaller rate constant (k' = 2.82×10^3 M^{-1} s^{-1}) with respect to **4** was obtained under catalytic conditions (0.4 M Ce^{IV}, see Supporting Information Figure S8).

Proposed Catalytic Cycles and Theoretical. On the basis of the combined experimental data for complexes **1**−**6**, key points are as follows: (i) using electrochemical methods,

dx.doi.org/10.1021/ja309805m | J. Am. Chem. Soc. 2012, 134, 18868−18880

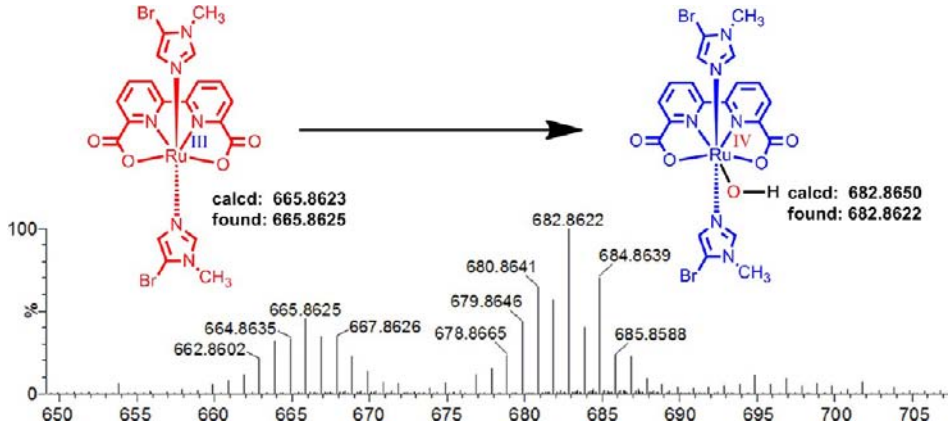

Figure 9. Mass spectra of Ru^{III} and Ru^{IV}−OH species related to complex **6**. The sample was immediately analyzed after adding 8 **eq** Ce^{IV} to a solution of **6** (2×10^{-5} M). The peaks found: m/z^+ = 665.8625 ($[Ru^{III}]^+$), m/z^+ = 682.8622 ($[Ru^{IV}-OH]^+$). After 1−2 min, the $[Ru^{IV}-OH]^+$ peak disappeared due its instability.

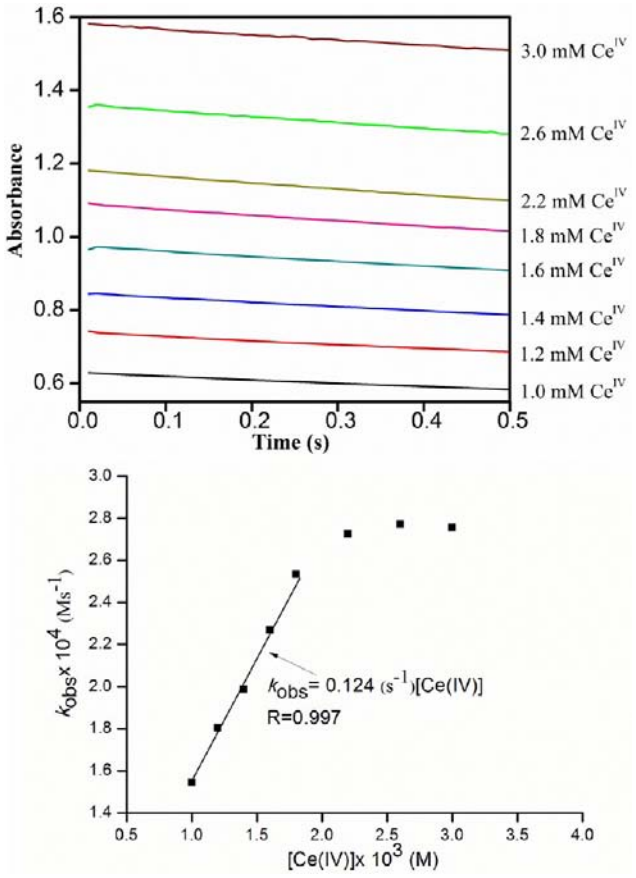

Figure 10. Above: Changing in absorption of Ce^{IV} monitoring at 360 nm after mixing complex **4** (0.01 mM) with different concentrations of Ce^{IV} aqueous solution under pH 1.0 conditions (0.1 M HNO_3). Below: Plots of k_{obs} (k_{obs} = initial rate. The initial rates were calculated by linear fitting the data from 0 to 0.5 s in the upper portion) vs $[Ce^{IV}]$. Ce^{IV} loss is first order in Ce^{IV} at $[Ce^{IV}] < \sim 2.0$ mM with a first-order rate constant of 0.124 s^{-1} and becomes to zero order in Ce^{IV} at higher concentrations of Ce^{IV}.

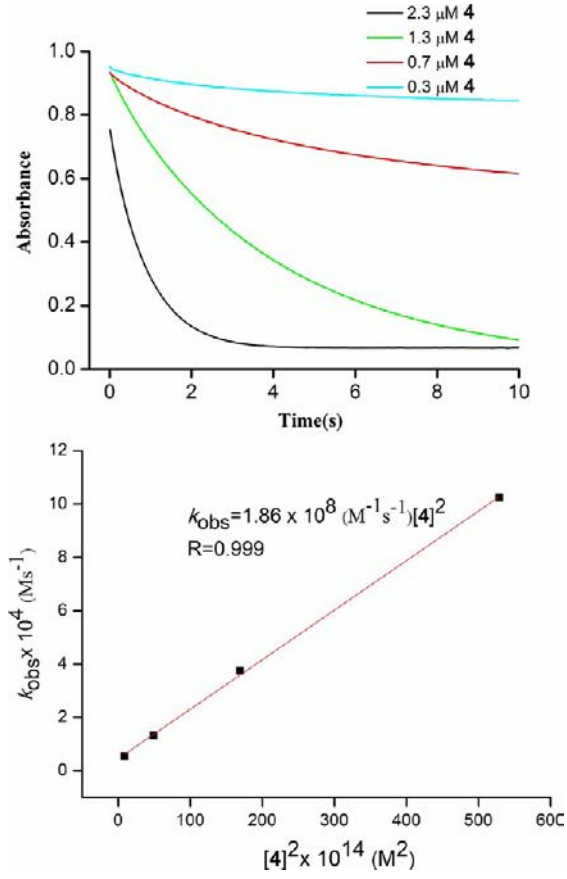

Figure 11. Above: Monitoring decay of Ce^{IV} at 360 nm after mixing different amount of complex **4** (2.3, 1.3, 0.7, 0.3 μM) with an aqueous solution of Ce^{IV}(1.667 mM) under pH 1.0 conditions (0.1 M HNO_3). Below: Plots of k_{obs} (The initial rates were calculated by linear fitting the data from 0 to 0.5 s in the upper figure in Figure 11) versus $[4]^2$. Ce^{IV} loss is second order in catalyst **4** with a second order rate constant of 1.86×10^8 M^{-1} s^{-1}.

the electron and proton transfer sequence of complex **4a** under acidic conditions has been found to follow $Ru^{II}-OH_2 \rightarrow Ru^{III}-OH_2 \rightarrow Ru^{IV}-OH \rightarrow Ru^{V}=O$, (ii) the second order rate law in catalysts for the Ce^{IV}-driven water oxidation reaction indicates a binuclear reaction pathway, most likely involving the O−O bond formation via the radical coupling of two Ru=O units, and (iii) detected by MS, the seven coordinate Ru^{IV}−OH intermediate, indicates that seven coordinate Ru intermediate is involved in the catalytic water oxidation. All these findings point to a common reaction mechanism for complexes **1**−**4**, which we have earlier proposed for [Ru(bda)-

dx.doi.org/10.1021/ja309805m | J. Am. Chem. Soc. 2012, 134, 18868−18880

L_2] (L = picoline and isoquinoline) complexes.[51] The essence of the mechanism is that Ru^V=O species are involved in the O−O bond formation via the radical coupling, forming a $[Ru^{IV}-O-O-Ru^{IV}]^{2+}$ peroxide with subsequent release of O_2 via a reduction elimination reaction. In addition to such a path way, the peroxide $[Ru^{IV}-O-O-Ru^{IV}]^{2+}$ could also be further oxidized by Ce^{IV}, as proposed based on DFT calculations and recent kinetics measurements via stopped-flow technique earlier,[51] to form a higher charged super oxide $[Ru^{IV}-O^{\bullet}O-Ru^{IV}]^{3+}$ which subsequently cleaved to $[Ru^{IV}-O=O]^{2+}$ and Ru^{III}, and subsequently $[Ru^{IV}-O=O]^{2+}$ releases O_2 as showed in Scheme 2.[51]

Scheme 2. Proposed Oxygen Generation Pathways under the Catalytic Conditions Use the Ce^{IV} as Oxidant under pH 1.0 Conditions

$$Ru^{II}-OH_2 + Ce^{IV} \xrightarrow{fast} Ru^{III}-OH_2 + Ce^{III} \quad (1)$$

$$Ru^{III}-OH_2 + Ce^{IV} \xrightarrow{fast} Ru^{IV}-OH + Ce^{III} + H^+ \quad (2)$$

$$Ru^{VI}-OH + Ce^{IV} \xrightarrow{k_3} Ru^{V}=O + Ce^{III} + H^+ \quad (3)$$

$$Ru^{V}=O + Ru^{V}=O \xrightarrow{k_{o-o}} Ru^{IV}-O-O-Ru^{IV} \quad (4)$$

Path A :

$$Ru^{IV}-O-O-Ru^{IV} + 2H_2O \xrightarrow{k_{O2}} 2Ru^{III}-OH_2 + O_2 \quad (5)$$

Path B :

$$Ru^{IV}-O-O-Ru^{IV} + Ce^{IV} \underset{k_{-6}}{\overset{k_6}{\rightleftharpoons}} Ru^{IV}-O^{\bullet}O-Ru^{IV} + Ce^{III} \quad (6)$$

$$Ru^{IV}-O^{\bullet}O-Ru^{IV} + H_2O \xrightarrow{k_7} Ru^{IV}-O=O + Ru^{III}-OH_2 \quad (7)$$

$$Ru^{IV}-O=O + H_2O \xrightarrow{k_{O2}} Ru^{IV}-OH + O_2 + H^+ \quad (8)$$

The observed reaction order change in Ce^{IV} from first order to zero order upon increasing [Ce^{IV}] (see the kinetic study section) is most likely due to that under high [Ce^{IV}] conditions the rate of eq 6 becomes faster than that of eq 4 and also the Nernstian effect on the $E_{Ce(IV)/Ce(III)}$. As a result, the rate determining step changes from the high charged super oxide $[Ru^{IV}-O^{\bullet}O-Ru^{IV}]^{3+}$ formation step (eq 6 in Scheme 2) to the O−O bond formation step (eq 4 in Scheme 2).

In light of a sizable difference in the performance between catalysts **4a** and **6**, that is, TOF(**4a**) ≫ TOF(**6**), and taking into account the experimentally observed kinetics of O_2 formation (see above) for both, we became motivated to model pathways which involve an interaction of two metal centers, the so-called I2M-pathway. Our goal is to meaningfully compare catalysts **4a** and **6** at the same level of the density functional theory,[55] also a question is whether (and to what extent) axial ligands can be involved in I2M-pathway. We have therefore first investigated complexes **4a** and **6** in aqueous environment from low, Ru^{II}, to high, formally Ru^V, oxidation states of ruthenium centers. We then proceeded to calculate I2M-pathways of the O−O bond formation.[56]

Monomeric Imidazole/DMSO−Ruthenium Complex 4a and Imidazole/Imidazole and Complex 6. Since DMSO has two different donor heteroatoms, in complexes such as **4a** it can in principle coordinate to ruthenium in two ways: via either Ru−S or Ru−O bonds. The concept that a match between ligand−metal donor−acceptor properties leads to a stronger metal−ligand bonding is often used to rationalize relative stability of organometallic complexes. The sulfur atom in DMSO is nucleophilic toward soft electrophiles and the oxygen is nucleophilic toward hard electrophiles. Thus, Ru^{II} center is expected to favor "softer" donor heteroatom of DMSO, that is, S atom, while Ru^{IV} and even more so formally Ru^V are both expected to favor "harder" donor heteroatom of DMSO, that is, O atom.[57] Our calculations are in agreement with the above hypothesis. In comparison with Ru^{II}−O alternative (Supporting Information Figure S10), Ru^{II}−S bonding (Figure 12) is favored by 2.7 kcal/mol. The calculated

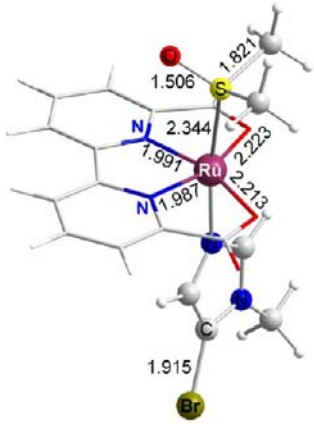

Figure 12. Calculated structures of the lowest-energy Ru^{II}-complex **4a** with the ruthenium−DMSO coordination via ruthenium−S bond. All distances are in Å.

structure with Ru^{II}−S coordination, Figure 12, has O−Ru−O cleft-angle of 124.18° and overall matches with the X-ray crystal structure. For the high oxidation state of ruthenium, that is, Ru^{IV}/Ru^V, ruthenium-O bonding of DMSO is favored over ruthenium-S alternative. To know better possible structures of mechanistically important Ru^V=O analogs of **4a**,[58] complexes with DMSO coordination via ruthenium−O and ruthenium−S bonds were calculated and from that we learned that ruthenium−O bonding of DMSO is favored over ruthenium−S analogs by 10.8 kcal/mol. Lowest-energy conformers with ruthenium-O bonding of DMSO, ***α*** and ***β***, are shown in Figure 13 A and B, the higher-energy ruthenium-S analog is shown in Supporting Information Figure S11. Coordination of DMSO to the formally Ru^V center via the ruthenium−oxygen bond is rather flexible in the sense that conformers (minima) with different orientation of DMSO have relatively similar energies. Among many calculated structures, the two mechanistically relevant low-energy minima are ***α*** and ***β***

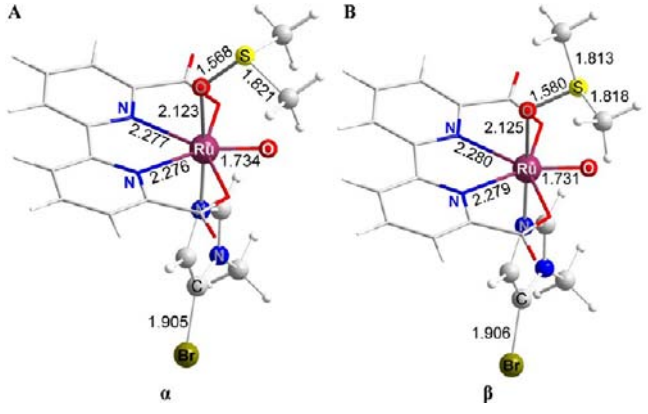

Figure 13. Calculated structures of two lowest-energy conformers of formally Ru^V=O analog of complex **4a** with DMSO coordination via ruthenium−O bond. All distances are in Å.

dx.doi.org/10.1021/ja309805m | J. Am. Chem. Soc. 2012, 134, 18868−18880

(Figure 13 A and B). Relative energy of β is 1.4 kcal/mol with respect to α.

The calculated Ru^{II} and formally Ru^{V}=O analogs of complex **6** are shown in Figure 14. As far as the coordination between

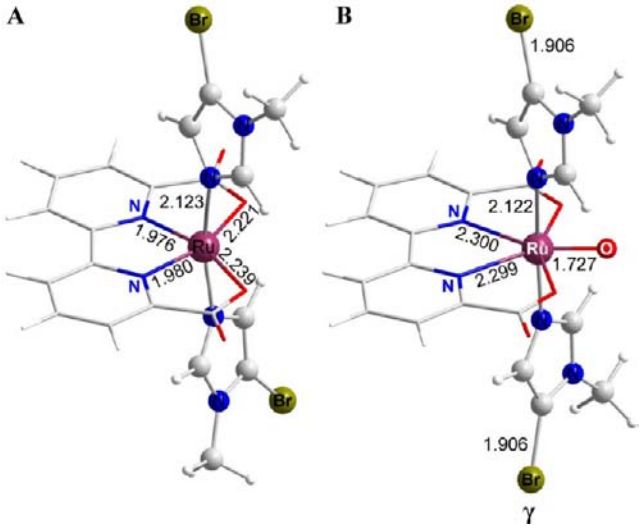

Figure 14. Calculated structures of the Ru^{II}-complex **6** (A) and formally Ru^{V}=O analog (B). All distances are in Å.

the equatorial ligand and ruthenium center is concerned, formally Ru^{V}=O complexes α, β and γ are much alike; the Ru−O bond length is in all three complexes ~1.73 Å but the terminal oxygen atom is apparently more accessible in complex β in comparison with complex α or γ. As we will see later on, the structure and the coordination mode of axial ligands affects the accessibility of the terminal oxygen atom and that will translate into an appreciable difference in the energetics of the radical coupling pathway.

Electrochemistry and the Electronic Structure of "Ru^{V}=O" Analogs of 4a and 6. The sequence of oxidation steps of Ru^{II} species in aqueous solution, electrochemically or oxidant driven, culminates with monoradical Ru^{V}=O active species. Taking guidance from experiment, we have calculated the sequence of oxidation steps, $Ru^{II}-OH_2 \rightarrow Ru^{III}-OH_2 \rightarrow Ru^{IV}-OH \rightarrow Ru^{V}=O$, following the now standard protocol details of which are provided in Supporting Information. For complex **4**, the Ru^{II}/Ru^{III} step is calculated to occur at 0.8 V versus NHE in aqueous environment treated as self-consistent reaction field. The proton coupled steps Ru^{III}/Ru^{IV} and Ru^{IV}/Ru^{V} correspond to the calculated potentials of about 1.2 V versus NHE and 1.5 V versus NHE, respectively. An agreement between calculated and experimental redox potentials is satisfactory. Also, similar consistency has been obtained for calculated redox potentials for complexes **6** and **2**. The main point here is not the exact match or mismatch of the calculated potentials with respect to experiment, but an overall consistency of the sequence of the oxidation steps and the potential at which an active species, formally Ru^{V}=O complex, is expected to be formed.

O−O Bond Formation. The shape of the singly occupied molecular orbital (SOMO) and spin density of imidazole/DMSO and imidazole/imidazole monoradicals α, β, and γ reveals distinctive oxyl character of terminal oxygen atom (see Supporting Information Figures S12 and S13). These monoradicals can react via the direct coupling of two metal−O units, the so-called interaction of two metal centers (I2M).

The potential energy profile of I2M-pathway, the total energy of a pair of interacting Ru^{V}=O monoradicals as a function of the decreasing distance between terminal oxygen atoms, was calculated following the protocol of our previous work (see ref 51 and Supporting Information for details). Direct interaction (coupling) of two Ru^{V}=O species gives the closed shell intermediate with two Ru^{IV}-centers bridged by the formally O_2^{2-} moiety, that is, a peroxo-dimer.[51] The high point of the apex of the potential energy profile is the transition state at the O−O distance of about 2.0 Å. Geometries of the transition state and the peroxo-dimer are related with regard to the relative arrangement of equatorial, as well as axial, ligands. For WOCs **4a** and **6**, key aspects of the calculated potential energy profile of I2M-pathways followed by the O_2-liberation are summarized in Scheme 3. The total in-aqua energy (including

Scheme 3. Pathway of the O−O Bond Formation and Subsequent Evolution of O_2 via Radical Coupling (I2M) in Water, WOCs 4a and 6[a]

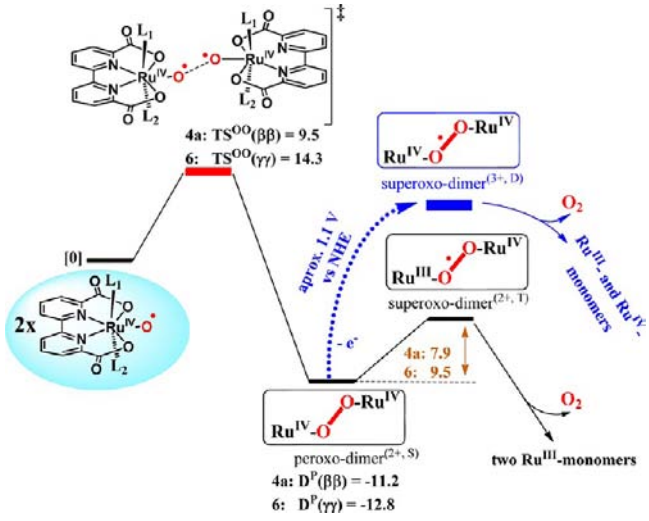

[a]Relative electronic energies in kcal/mol are shown in square brackets, see text regarding the definition of the reference energy (zero point of the energy scale). The dotted blue line represent herein proposed oxidation step (the calculated potential is in V versus NHE).

solvent effects) of the pair of formally Ru^{V}=O complexes at a large distance between terminal oxygen atoms, for example, O−O ≥ 3 Å, is nearly identical to twice the individual in-aqua energy of formally Ru^{V}=O complex. That is the reference energy, or "zero point", in Scheme 3.

The deceivingly simple energy-diagram of I2M-pathways for catalysts **4a** and **6**, Scheme 3, has a computationally intensive underpinning (see details in Supporting Information).[59] Depending on the structure and electronic properties of axial ligands, their involvement can either facilitate I2M-pathway, as we have just recently suggested, or hinder it by means of "trivial" steric hindrance.[51]

Based on a systematic evaluation of plausible coupling pathways for α and β conformers of active analogs of **4a**,[60,61] the lowest energy dimer, $D^{P}(\beta\beta)$ (Figure 15), has been found on the singlet state potential energy surface. Not surprisingly, each of the two DMSO molecules in $D^{P}(\beta\beta)$ is oriented in such a way that steric congestion is as little as possible. Each of the

dx.doi.org/10.1021/ja309805m | J. Am. Chem. Soc. 2012, 134, 18868−18880

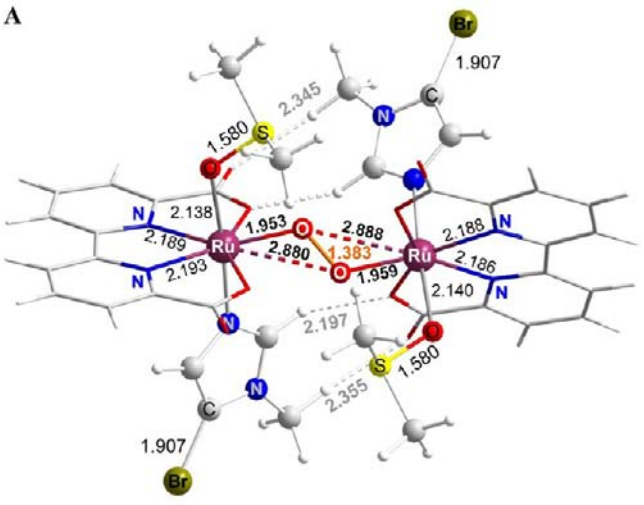

Figure 15. Calculated structure of the peroxo-dimers as a result of the radical coupling $\beta + \beta \rightarrow D^P(\beta\beta)$ and $\alpha + \alpha \rightarrow D^P(\alpha\alpha)$. All distances are in Å.

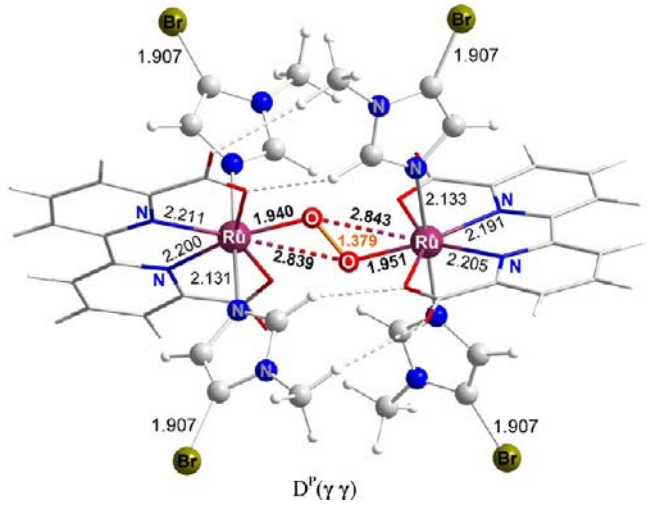

Figure 16. Calculated structure of the peroxo-dimer for catalyst **6** (the result of the radical coupling $\gamma + \gamma \rightarrow D^P(\gamma\,\gamma)$. All distances are in Å.

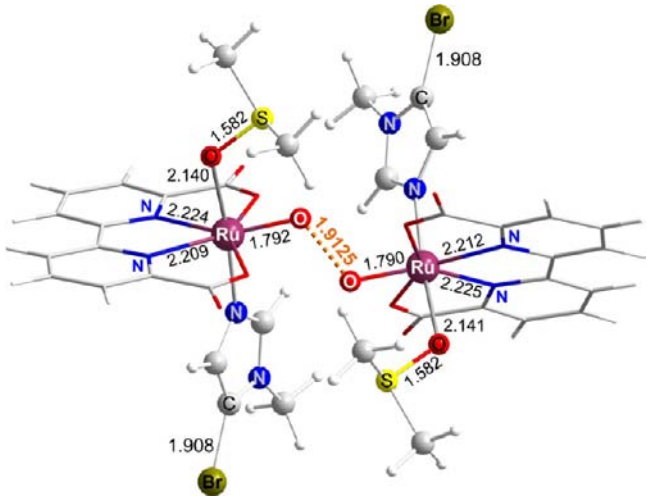

Figure 17. Calculated structure of $TS^{OO}(\beta\beta)$ at the apex of the potential energy profile of the O−O bond formation via I2M-pathway $\beta + \beta \rightarrow D^P(\beta\beta)$. All distances are in Å.

two "halves" of $D^P(\beta\beta)$ resembles complex $\boldsymbol{\beta}$; the resultant dimer formally corresponds to $\boldsymbol{\beta} + \boldsymbol{\beta} \rightarrow D^P(\beta\beta)$ coupling. Among all too many plausible conformers which were systematically sampled, we have also found peroxo dimers, such as $D^P(\alpha\alpha)$ (Figure 15). Despite having higher total energy than $D^P(\beta\beta)$,[62] $D^P(\alpha\alpha)$ is mechanistically interesting as it formally corresponds to coupling $\boldsymbol{\alpha} + \boldsymbol{\alpha} \rightarrow D^P(\alpha\alpha)$ without the reorientation of DMSO. According to our calculations, $E\{D^P(\beta\beta)\} < E\{D^P(\alpha\beta)\} < E\{D_p(\alpha\alpha)\}$.

The calculated peroxo-dimer for catalyst **6**, $\boldsymbol{\gamma} + \boldsymbol{\gamma} \rightarrow D^P(\boldsymbol{\gamma}\,\boldsymbol{\gamma})$, is shown in Figure 16.

At the transition state area, denoted by an apex of the potential energy profile, the effect of the orientation of DMSO upon the total energy of transient structures did not exceed 2.5 kcal/mol. From systematic calculations, we can conclude that $E\{\mathbf{TS}^{OO}(\beta\beta)\} < E\{\mathbf{TS}^{OO}(\boldsymbol{\alpha}\beta) < E\{\mathbf{TS}^{OO}(\boldsymbol{\alpha\alpha})\}$. All details regarding the potential energy profile calculations can be found in Supporting Information. The transition state $\mathbf{TS}^{OO}(\beta\beta)$ (Figure 17) with O−O distance of about 1.913 Å was found at an apex of the calculated potential energy profile $\beta + \beta \rightarrow D^P(\beta\beta)$. Similarly to $D^P(\beta\beta)$, each of the two DMSO molecule in $\mathbf{TS}^{OO}(\beta\beta)$ is oriented in such a way that an steric congestion (collisions) are minimized (avoided). Calculation of vibrational frequencies of $\mathbf{TS}^{OO}(\beta\beta)$ revealed the strictly single imaginary igenvalue, −173.3 cm^{-1}. Upon visual inspection of the animation of the corresponding normal vibrational mode, a proper O−O bonding motion has been seen. At the transition state, SOMO−SOMO interaction between formally Ru^V=O complexes is a mechanistically significant aspect of the electronic structure. The bonding and the corresponding antibonding (unoccupied) orbitals of the O−O bonding transition state are shown in Figure S14 in Supporting Information.

The O−O bond formation transition state, $\mathbf{TS}^{OO}(\gamma\gamma)$, for catalyst **6** is shown in Supporting Information Figure S15 with two molecular orbitals generated by SOMO−SOMO interaction. Although quite similar to $\mathbf{TS}^{OO}(\beta\beta)$ at the electronic level, the structure of $\mathbf{TS}^{OO}(\gamma\gamma)$ suggests collision of axial and equatorial ligands, which makes it more difficult for terminal

dx.doi.org/10.1021/ja309805m | J. Am. Chem. Soc. 2012, 134, 18868−18880

oxygen atoms to interact. Hence, $TS^{OO}(\gamma\gamma)$ is appreciably higher in energy in comparison with $TS^{OO}(\beta\beta)$.

The peroxo-dimer, as an intermediate in the I2M-pathway, is important from the mechanistic point of view. Here-in calculated structures, the distance between oxygen atoms of the bridging fragment is about 1.38 Å, which is consistent with our earlier calculations. The torsion angle between the planes of equatorial ligands is about 40°. Also, since we have performed analysis of conformers both of the apex of potential energy profile and of the peroxo-dimer, it became clear to us that formally the lowest energy transition state of I2M-pathway bears strong structural similarity with the formally lowest energy peroxo dimer. At the transition state, as we learned from the molecular orbital analysis, SOMO−SOMO overlap is the key molecular orbital interaction hence the apex of the I2M pathway feature quite similar O−O distance for both complexes calculated. The structure of the optimal transition is a product of a compromise between largest SOMO−SOMO orbital overlap, that is, stability of the forming bonding orbital, and lowest possible sterical collision of axial/equatorial ligands. This implies, we think, that the fully optimal I2M-pathway involves as little reorganization of the relative positioning of interacting complexes as possible so that the peroxo bridge could be formed in the most straightforward manner. In our opinion, based on I2M-pathway calculation with analysis of conformers of key mechanistic points, favors the transition state of radical coupling for complexes with one axial DMSO molecule where coordination to ruthenium center is flexible enough to accommodate demands of reduced steric collisions at the transition state. That being said, the electronic structure of the dioxygen bridge itself by large is unaffected by the nature of axial ligands; it corresponds to the fully closed shell configuration. This places it in access of two electrons as compared to the expected final state of the molecular oxygen upon release, which is triplet, from the peroxo-dimer.

O_2-Liberation: Two Pathways via Different Superoxo-Dimers. For both WOCs **4a** and **6**, we would now like to consider O_2-liberation pathway via electronically (and structurally) different superoxo dimers (Scheme 3). Peroxo-dimers from Scheme 3 have charge +2 and a closed shell singlet electronic states, henceforth referred to as peroxo-dimer$^{(2+,\,S)}$. From peroxo-dimer$^{(2+,\,S)}$, the O_2-liberation has been proposed to involve the so-called superoxo-dimer$^{(2+,\,T)}$ in which one ruthenium is reduced to Ru^{III} while the O_2^{2-} bridging fragment is oxidized toward the anionic O_2^- bridge. Structural difference between peroxo-dimer$^{(2+,\,S)}$ and superoxo-dimer$^{(2+,\,T)}$ stems from the difference in oxidation states of ruthenium centers and the electronic structure of the dioxygen bridge. The energy difference between these two fully optimized dimers of the same charge, +2, but a different spin state is relatively small for both WOCs **4a** and **6** (see Scheme 3). The key feature of the electronic structure of superoxo-dimer$^{(2+,\,T)}$ is the spin-density distribution: one partially occupied π^*2p orbital of O_2^- fragment and d5-configuration a ruthenium center with one unpaired electron. For example, for WOC **4a** the calculated spin density distribution in superoxo-dimer$^{(2+,\,T)}$ is shown in Figure 18.

In agreement with results from our earlier work, peroxo-dimer$^{(2+,\,S)}$ is quite stable with regard to a structural perturbation of the Ru−OO−Ru closed shell bridge at the vicinity of the calculated equilibrium. On the contrary, the Ru−OO−Ru bridge shows signs of nonequivalent Ru−O bonds and as a whole the superoxo-dimer$^{(2+,\,T)}$ is confined in a rather

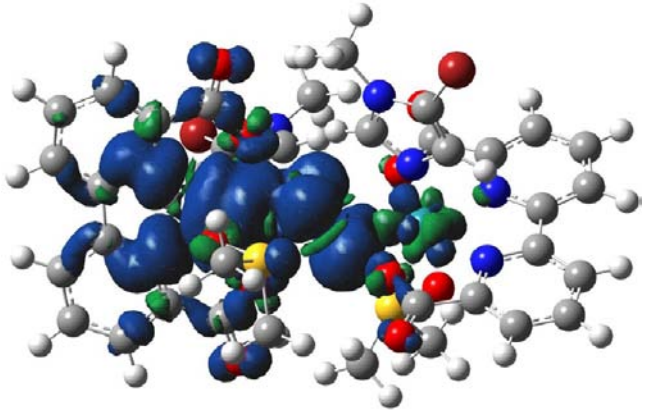

Figure 18. Spin density of the superoxo-dimer$^{(2+,\,T)}$ (triplet electronic state) for WOC **4a**.

shallow potential well. A minor structural perturbation of superoxo-dimer$^{(2+,\,T)}$ leads it onto the dissociative region of the triplet potential energy surface. As the slightly perturbed superoxo-dimer$^{(2+,\,T)}$ evolves in that region, the Ru−OO−Ru bridge breaks via the stepwise scission of the Ru−O bonds in the course of a geometry optimization. First, Ru−OO−Ru cleaves into Ru-OO and Ru^{III} species. As the geometry optimization continues, the remaining Ru−O bond cleaves. In the end, the result is the reduction of Ru^{IV} centers and the complete dissociation of Ru−O bonds with the release of the O_2 molecule and liberation of two Ru^{III}-monomers. The successive fashion of the two steps of the cleavage of the metal−oxygen bonds in the Ru-OO-Ru bridge has been seen in all geometry optimizations starting from different perturbed superoxo-dimer$^{(2+,\,T)}$ initial structures, which is also in accordance with our earlier results. In support of the mechanistic scenario involving superoxo-dimer$^{(2+,\,T)}$, see the comparison of our earlier calculations with recent experimental data based on stopped-flow measurement.[51]

An alternative pathway of O_2-evolution is as follows. Based on the peroxo-dimer$^{(2+,\,S)}$ with two Ru^{IV} centers we have found it is analog after one-electron oxidation. According to calculations, the removal of one electron from the Ru^{IV} peroxo-dimer$^{(2+,\,S)}$, peroxo-dimer$^{(2+,\,S)}$ + Ce^{IV} → superoxo-dimer$^{(3+,\,D)}$ + Ce^{III}, results in the oxidation of the O_2^{2-} cationic bridge toward the superoxide (O_2^-) while each of the two ruthenium centers remains in the Ru^{IV} state in the peroxo-dimer$^{(3+,\,D)}$. According to Mulliken spin populations, there is no significant unpaired spin density on neither of two ruthenium centers, effectively ruling out[10] electronic structure. The unpaired electron is instead shared by the oxygen atoms of the superoxide (O_2^-) bridge. The spin density (Figure 19 for WOC **4a** as an example) corresponds to $[Ru^{IV}-O^{\bullet}O-Ru^{IV}]^{3+}$ electronic state. In water, the calculated potential for the $[Ru^{IV}-OO-Ru^{IV}]^{2+}$ → $[Ru^{IV}-O^{\bullet}O-Ru^{IV}]^{3+}$ process is approximately 1.1 V versus NHE at pH 1.0 for both WOCs **4a** and **6**, well within the reach of the Ce^{IV}. From the $[Ru^{IV}-O^{\bullet}O-Ru^{IV}]^{3+}$ dimer, O_2 is liberated in a facile manner via dissociative disproportionation into Ru^{III} and Ru^{IV} fragments (Scheme 3).

The relative likelihood of the occurrence of one or the other O_2-liberation pathway via different superoxo-dimers cannot yet be fully determined from our calculations alone mainly because these two pathways imply meaningfully different experimental conditions. Considering results from theory and experiment

dx.doi.org/10.1021/ja309805m | J. Am. Chem. Soc. 2012, 134, 18868−18880

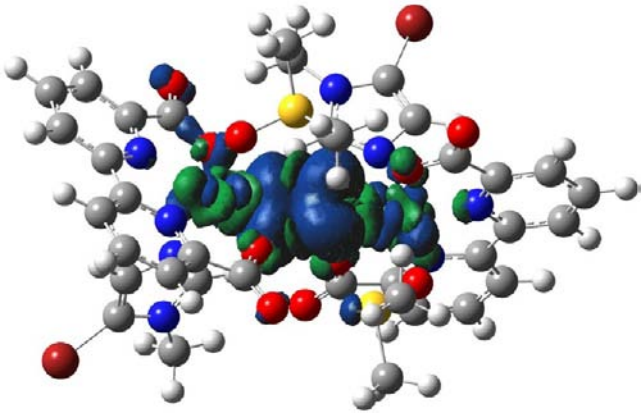

Figure 19. Spin density of the superoxo-dimer$^{(3+,\,d)}$ (doublet electronic state) for WOC **4a**.

combined, it appears that the pathway via superoxo-dimer$^{(2+,\,T)}$ is particularly suitable to describe the situation at low Ce concentrations, while the pathway via superoxo-dimer$^{(3+,\,D)}$ relates to the process at much higher Ce^{IV} concentrations.

CONCLUSIONS

Here we report synthesis of a series of Ru-based WOCs (**1**−**6**) using 2,2′-bipyridine-6,6′-dicarboxylate and imidazole/DMSO as coordinating ligands, as well as, a detailed structural and electrochemical characterization of all complexes and results of the combined experimental and theoretical investigations of their catalyst activity. For complexes **1**−**4**, DMSO-coordinates to ruthenium as one of the axial ligands, bda coordinates to ruthenium in a tridentate fashion. According to both ^{1}H NMR and MS, the imidazole ligand dissociates under the catalytic conditions (pH 1), in situ forming what we regard as an active complexes (**1a**−**4a**) with the Ru^{II} center. Complexes **1**−**4** show high efficiency for water oxidation in homogeneous systems using Ce^{IV} as the oxidant. For example, for complexes **1**−**4** the initial turnover frequency exceeds 100 s^{-1}. Compared with the control complex **6** which has the imidazole/imidazole as an axial ligand combination, DMSO/imidazole is an axial ligand combination in complex **4a**. This change corresponds to a sizable increase of the catalytic activity of **4a** in comparison with that of **6**. According to calculations, the key difference between WOCs **4a** and **6** is in the ability of axial ligands to allow unhindered coupling between terminal oxygen atoms, this is the reason for the high efficiency of complexes **1a**−**4a**. The difference between electronic properties of herein reported complexes appears to be a secondary factor in comparison with steric effects related to the structure and the coordination mode of axial ligands.

An attractive way to prepare anodic electrodes of water splitting devices is the immobilization of a homogeneous WOC on the electrode surface. This could allow catalysis of water oxidation under milder conditions, for example, neutral solutions which could considerably favor water oxidation and protect the ligand from the oxidative decomposition. The efficiency of recently developed prototype water splitting devices is yet to reach its full potential, primarily because of lower than necessary activity of WOCs employed. Thus, building up highly efficient water splitting devices goes hand in hand with the develop of highly active WOCs and their further improvement.[50] Our results reveal intriguing structure−activity relations which could be of help in the design and synthesis of even efficient catalyst for oxygen generation which can be utilized in an advanced water splitting device.

ASSOCIATED CONTENT

Supporting Information

CIF file for complex **4a**, NMR, MS spectra, electrochemistry, and the catalytic data for these complexes, computational methods, and details. This material is available free of charge via the Internet at http://pubs.acs.org.

AUTHOR INFORMATION

Corresponding Author

*E-mail: liujh@dlut.edu.cn (J.L.); priti@organ.su.se (T.P.); lichengs@kth.se (L.S.).

Notes

The authors declare no competing financial interest.

ACKNOWLEDGMENTS

The Swedish Research Council, K & A Wallenberg Foundation, the Swedish Energy Agency, China Scholarship Council (CSC), National Natural Science Foundation of China (20633020, 21120102036) and National Basic Research Program of China (2009CB220009) supported this work. We are also grateful to Dr. Lin Chen for his help on crystal structure.

REFERENCES

(1) Lewis Nathan, S.; Nocera Daniel, G. *Proc. Natl. Acad. Sci. U. S. A.* **2006**, *103*, 15729.
(2) Nocera, D. G. *ChemSusChem* **2009**, *2*, 387.
(3) Meyer, T. J. *Nature (London, U. K.)* **2008**, *451*, 778.
(4) Yagi, M.; Kaneko, M. *Chem. Rev. (Washington, D. C.)* **2001**, *101*, 21.
(5) Muckerman, J. T.; Polyansky, D. E.; Wada, T.; Tanaka, K.; Fujita, E. *Inorg. Chem. (Washington, DC, U. S.)* **2008**, *47*, 1787.
(6) Gust, D.; Moore, T. A.; Moore, A. L. *Acc. Chem. Res.* **2009**, *42*, 1890.
(7) Sala, X.; Romero, I.; Rodriguez, M.; Escriche, L.; Llobet, A. *Angew. Chem., Int. Ed.* **2009**, *48*, 2842.
(8) Sun, L.; Hammarstrom, L.; Akermark, B.; Styring, S. *Chem. Soc. Rev.* **2001**, *30*, 36.
(9) Gersten, S. W.; Samuels, G. J.; Meyer, T. J. *J. Am. Chem. Soc.* **1982**, *104*, 4029.
(10) Gilbert, J. A.; Eggleston, D. S.; Murphy, W. R., Jr.; Geselowitz, D. A.; Gersten, S. W.; Hodgson, D. J.; Meyer, T. J. *J. Am. Chem. Soc.* **1985**, *107*, 3855.
(11) Leung, C.-F.; Ng, S.-M.; Ko, C.-C.; Man, W.-L.; Wu, J.; Chen, L.; Lau, T.-C. *Energy Environ. Sci.* **2012**, *5*, 7903.
(12) Berardi, S.; La Ganga, G.; Natali, M.; Bazzan, I.; Puntoriero, F.; Sartorel, A.; Scandola, F.; Campagna, S.; Bonchio, M. *J. Am. Chem. Soc.* **2012**, *134*, 11104.
(13) Wasylenko, D. J.; Ganesamoorthy, C.; Borau-Garcia, J.; Berlinguette, C. P. *Chem. Commun.* **2011**, *47*, 4249.
(14) Zhu, G.; Geletii, Y. V.; Kogerler, P.; Schilder, H.; Song, J.; Lense, S.; Zhao, C.; Hardcastle, K. I.; Musaev, D. G.; Hill, C. L. *Dalton Trans.* **2012**, *41*, 2084.
(15) McCool, N. S.; Robinson, D. M.; Sheats, J. E.; Dismukes, G. C. *J. Am. Chem. Soc.* **2011**, *133*, 11446.
(16) Dogutan, D. K.; McGuire, R.; Nocera, D. G. *J. Am. Chem. Soc.* **2011**, *133*, 9178.
(17) Duan, L.; Fischer, A.; Xu, Y.; Sun, L. *J. Am. Chem. Soc.* **2009**, *131*, 10397.
(18) Rotzinger, F. P.; Munavalli, S.; Comte, P.; Hurst, J. K.; Graetzel, M.; Pern, F. J.; Frank, A. J. *J. Am. Chem. Soc.* **1987**, *109*, 6619.
(19) Zong, R.; Thummel, R. P. *J. Am. Chem. Soc.* **2005**, *127*, 12802.
(20) Geletii, Y. V.; Huang, Z.; Hou, Y.; Musaev, D. G.; Lian, T.; Hill, C. L. *J. Am. Chem. Soc.* **2009**, *131*, 7522.

(21) Tong, L.; Duan, L.; Xu, Y.; Privalov, T.; Sun, L. *Angew. Chem., Int. Ed.* **2011**, *50*, 445.
(22) Tseng, H.-W.; Zong, R.; Muckerman, J. T.; Thummel, R. *Inorg. Chem. (Washington, DC, U. S.)* **2008**, *47*, 11763.
(23) Duan, L.; Xu, Y.; Gorlov, M.; Tong, L.; Andersson, S.; Sun, L. *Chem.—Eur. J.* **2010**, *16*, 4659.
(24) Deng, Z.; Tseng, H.-W.; Zong, R.; Wang, D.; Thummel, R. *Inorg. Chem. (Washington, DC, U. S.)* **2008**, *47*, 1835.
(25) Radaram, B.; Ivie, J. A.; Singh, W. M.; Grudzien, R. M.; Reibenspies, J. H.; Webster, C. E.; Zhao, X. *Inorg. Chem. (Washington, DC, U. S.)* **2011**, *50*, 10564.
(26) Yagi, M.; Tajima, S.; Komi, M.; Yamazaki, H. *Dalton Trans.* **2011**, *40*, 3802.
(27) Yamazaki, H.; Hakamata, T.; Komi, M.; Yagi, M. *J. Am. Chem. Soc.* **2011**, *133*, 8846.
(28) Boyer, J. L.; Polyansky, D. E.; Szalda, D. J.; Zong, R.; Thummel, R. P.; Fujita, E. *Angew. Chem., Int. Ed.* **2011**, *50*, 1.
(29) Wasylenko, D. J.; Ganesamoorthy, C.; Henderson, M. A.; Koivisto, B. D.; Osthoff, H. D.; Berlinguette, C. P. *J. Am. Chem. Soc.* **2010**, *132*, 16094.
(30) Polyansky, D. E.; Muckerman, J. T.; Rochford, J.; Zong, R.; Thummel, R. P.; Fujita, E. *J. Am. Chem. Soc.* **2011**, *133*, 14649.
(31) Tong, L.; Wang, Y.; Duan, L.; Xu, Y.; Cheng, X.; Fischer, A.; Ahlquist, M. S. G.; Sun, L. *Inorg. Chem.* **2012**, *51*, 3388.
(32) McDaniel, N. D.; Coughlin, F. J.; Tinker, L. L.; Bernhard, S. *J. Am. Chem. Soc.* **2008**, *130*, 210.
(33) Hull, J. F.; Balcells, D.; Blakemore, J. D.; Incarvito, C. D.; Eisenstein, O.; Brudvig, G. W.; Crabtree, R. H. *J. Am. Chem. Soc.* **2009**, *131*, 8730.
(34) Blakemore, J. D.; Schley, N. D.; Balcells, D.; Hull, J. F.; Olack, G. W.; Incarvito, C. D.; Eisenstein, O.; Brudvig, G. W.; Crabtree, R. H. *J. Am. Chem. Soc.* **2010**, *132*, 16017.
(35) Ellis, W. C.; McDaniel, N. D.; Bernhard, S.; Collins, T. J. *J. Am. Chem. Soc.* **2010**, *132*, 10990.
(36) Hurst, J. K.; Cape, J. L.; Clark, A. E.; Das, S.; Qin, C. *Inorg. Chem. (Washington, DC, U. S.)* **2008**, *47*, 1753.
(37) Gao, Y.; Aakermark, T.; Liu, J.; Sun, L.; Aakermark, B. *J. Am. Chem. Soc.* **2009**, *131*, 8726.
(38) Pecoraro, V. L.; Hsieh, W.-Y. *Inorg. Chem. (Washington, DC, U. S.)* **2008**, *47*, 1765.
(39) Liu, F.; Concepcion, J. J.; Jurss, J. W.; Cardolaccia, T.; Templeton, J. L.; Meyer, T. J. *Inorg. Chem. (Washington, DC, U. S.)* **2008**, *47*, 1727.
(40) Yamada, H.; Siems, W. F.; Koike, T.; Hurst, J. K. *J. Am. Chem. Soc.* **2004**, *126*, 9786.
(41) Nyhlen, J.; Duan, L.; Aakermark, B.; Sun, L.; Privalov, T. *Angew. Chem., Int. Ed.* **2010**, *49*, 1773.
(42) Sameera, W. M. C.; McKenzie, C. J.; McGrady, J. E. *Dalton Trans.* **2011**, *40*, 3859.
(43) Concepcion, J. J.; Tsai, M.-K.; Muckerman, J. T.; Meyer, T. J. *J. Am. Chem. Soc.* **2010**, *132*, 1545.
(44) Murakami, M.; Hong, D.; Suenobu, T.; Yamaguchi, S.; Ogura, T.; Fukuzumi, S. *J. Am. Chem. Soc.* **2011**, *133*, 11605.
(45) Romain, S.; Bozoglian, F.; Sala, X.; Llobet, A. *J. Am. Chem. Soc.* **2009**, *131*, 2768.
(46) Reece, S. Y.; Hamel, J. A.; Sung, K.; Jarvi, T. D.; Esswein, A. J.; Pijpers, J. J. H.; Nocera, D. G. *Science (Washington, DC, U. S.)* **2011**, *334*, 645.
(47) Youngblood, W. J.; Lee, S.-H. A.; Kobayashi, Y.; Hernandez-Pagan, E. A.; Hoertz, P. G.; Moore, T. A.; Moore, A. L.; Gust, D.; Mallouk, T. E. *J. Am. Chem. Soc.* **2009**, *131*, 926.
(48) Youngblood, W. J.; Lee, S.-H. A.; Maeda, K.; Mallouk, T. E. *Acc. Chem. Res.* **2009**, *42*, 1966.
(49) Brimblecombe, R.; Koo, A.; Dismukes, G. C.; Swiegers, G. F.; Spiccia, L. *J. Am. Chem. Soc.* **2010**, *132*, 2892.
(50) Li, L.; Duan, L.; Xu, Y.; Gorlov, M.; Hagfeldt, A.; Sun, L. *Chem. Commun. (Cambridge, U. K.)* **2010**, *46*, 7307.
(51) Duan, L.; Bozoglian, F.; Mandal, S.; Stewart, B.; Privalov, T.; Llobet, A.; Sun, L. *Nat. Chem.* **2012**, *4*, 418.
(52) Yin, Q.; Tan, J. M.; Besson, C.; Geletii, Y. V.; Musaev, D. G.; Kuznetsov, A. E.; Luo, Z.; Hardcastle, K. I.; Hill, C. L. *Science (Washington, DC, U. S.)* **2010**, *328*, 342.
(53) Dulière, E.; Devillers, M.; Marchand-Brynaert, J. *Organometallics* **2003**, *22*, 804−811.
(54) Holden, K. G.; Mattson, M. N.; Cha, K. H.; Rapoport, H. *J. Org. Chem.* **2002**, *67*, 5913.
(55) See Supporting Information for computational details and references. All reported relative energies account for solvent effects (self-consistent reaction-field representation of aqueous environment).
(56) The potential energy profile of I2M-pathway for complexes **4a** and **6** have been calculated following the successful protocol of our previous work (see ref 51 and Supporting Information for details).
(57) According to our calculations of RuII and RuIV of complex **4a**, the flip of the DMSO, that is, the change from Ru−S to Ru−O coordination and vice versa, requires to cross a relatively low-energy barrier of approximately 12 kcal/mol (see details in Supporting Information).
(58) For clarity, the formal electron count is used.
(59) Calculation of potential energy profiles for both WOCs **4a** and **6** was carried out with careful evaluation of plausible conformers (see also ref 51 as well as Supporting Information).
(60) Total energies of a considerable number of calculated structures (local minima) with different orientation of axial ligands, that is, imidazoles and DMSOs, have been compared. At the bottom of this energy-distribution, we have found about 40 structures that differed by the orientation of DMSO. Those were reoptimized and re-evaluated at an increased level of accuracy, see more details in Supporting Information.
(61) The axial imidazole ligands were much less computationally challenging in comparison with the computational complications brought by axial DMSO molecules.
(62) See also an example of the $\alpha\beta$-type of the peroxo dimer, DP($\alpha\beta$), shown in Supporting Information.